

SCIENTIFIC REPORTS



OPEN

Assembling Bare Au Nanoparticles at Positively Charged Templates

Wenjie Wang¹, Honghu Zhang^{1,2}, Ivan Kuzmenko³, Surya Mallapragada^{1,4} & David Vaknin^{1,5}

Received: 03 March 2016

Accepted: 04 May 2016

Published: 26 May 2016

In-situ X-ray reflectivity (XRR) and grazing incidence X-ray small-angle scattering (GISAXS) reveal that unfunctionalized (bare) gold nanoparticles (AuNP) spontaneously adsorb to a cationic lipid template formed by a Langmuir monolayer of DPTAP (1,2-dihexadecanoyl-3-trimethylammonium-propane) at vapor/aqueous interfaces. Analysis of the XRR yields the electron density profile across the charged-interfaces along the surface normal showing the AuNPs assemble with vertical thickness comparable to the particle size. The GISAXS analysis indicates that the adsorbed mono-particle layer exhibits short-range in-plane correlations. By contrast, single-stranded DNA-functionalized AuNPs, while attracted to the positively charged surface (more efficiently with the addition of salt to the solution), display less in-plane regular packing compared to bare AuNPs.

Langmuir monolayers assembled with insoluble, amphiphilic organic molecules, exhibiting rich phase behaviors, have been studied extensively as a model two dimensional (2D) systems for decades¹. Surface X-ray scattering techniques, such as specular reflectivity (XRR) and grazing incidence diffraction (GIXD), have played a decisive role in relating the phase behaviors, generally obtained from surface-pressure versus molecular area ($\pi - A$) isotherms, to the structure of the monolayer at unprecedented molecular length scales². The 2D nature of orderly Langmuir monolayers has inspired their use as templates to induce the growth of 2D organic and inorganic crystals³. On different length scales, 2D reversible clustering, and ordering of uniform colloidal particles have been accomplished by trapping them at air/water interfaces⁴⁻⁷. Subsequently, charged vesicle surfaces have been used to assemble colloidal particles in solutions⁸. More recently, NP self-assembly has been achieved and even though at times straightforward, it can be complicated by the interplay between these particles and their immediate environment that can be different than that in the bulk-medium (i.e., pH and salt concentrations near NP surfaces)⁹⁻¹¹. In fact, the same properties are used to disperse and stabilize AuNPs in aqueous solutions, either by electrostatic repulsion or steric forces¹¹. Spontaneous 2D assembly and crystallization of functionalized (capped) AuNPs with ssDNA by adjusting salt concentrations have been reported recently¹²⁻¹⁴. Similarly ssDNA-capped-AuNP have been assembled and crystallized at charged Langmuir monolayers with the goal to produce 2D meta-materials as an alternative to common top-down lithographical approach^{15,16}. In this study, we explore the interplay of the two key components of template-directed self-assembly, AuNPs as building blocks and a cationic lipid monolayer, i.e. 1,2-dihexadecanoyl-3-trimethylammonium-propane (DPTAP), as the template. The motivation of this two-dimensional model-system study is to explore underlying control parameters that can be exploited by design to assemble regular structures from nano-particles. We also demonstrate the application of synchrotron based X-ray liquid surface scattering techniques, i.e., specular reflectivity and grazing incidence scattering, and provide analytical tools to analyze similar GISAXS data in general.

Results and Discussion

Small-angle X-ray scattering (SAXS). Solution SAXS provides the actual size information of independent particles suspended in dilute solutions. The single AuNP is modeled as a solid sphere of radius R . Its scattering intensity can be expressed as $|\mathcal{F}|^2$, where \mathcal{F} is the form factor for a solid sphere of excess scattering length density, $\Delta\rho$, expressed as¹⁷

¹Division of Materials Sciences and Engineering, Ames Laboratory, USDOE, Ames, Iowa 50011, United States.

²Department of Materials Science and Engineering, Iowa State University, Ames, Iowa 50011, United States. ³X-ray Science Division, Advanced Photon Source, Argonne National Laboratory, Lemont, Illinois 60439, United States.

⁴Department of Chemical and Biological Engineering, Iowa State University, Ames, Iowa 50011, United States.

⁵Department of Physics and Astronomy, Iowa State University, Ames, Iowa 50011, United States. Correspondence and requests for materials should be addressed to W.W. (email: wwang@ameslab.gov) or D.V. (email: vaknin@ameslab.gov)

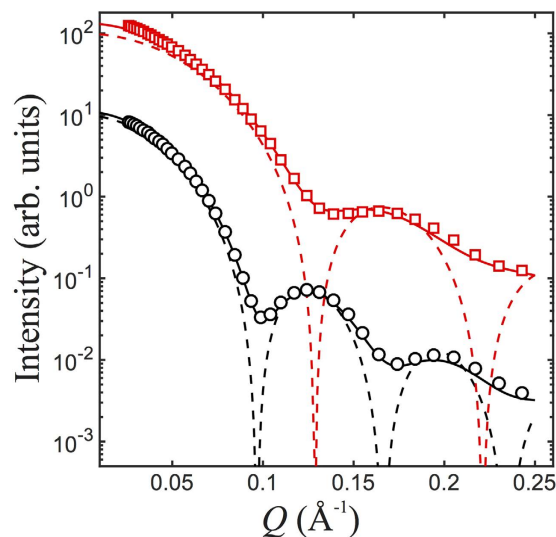


Figure 1. 1D SAXS data for suspended AuNPs in solutions. Black circles and red squares represent the data from AuNP of nominal diameter 10 and 5 nm, respectively. The solid lines and dashed lines are calculated intensity profiles from polydisperse and monodisperse spheres, respectively. The intensity data are re-scaled for display purpose.

Nominal diameter(Å) ^a	$2\langle R \rangle$ (Å)	$2\Delta R$ (Å)
100	89	8
50	65	10

Table 1. Particle size distribution determined with model refinement of SAXS data in terms of Eq. (2).

^aNominal diameters of the AuNPs are provided by the manufacturer Ted Pella, Inc.

$$\mathcal{F}(Q, R) = \left(\Delta\rho \cdot \frac{4}{3}\pi R^3 \right) \frac{3[\sin(Q \cdot R) - Q \cdot R(Q \cdot R)]}{Q^3 R^3} \quad (1)$$

The $|\mathcal{F}(Q, R)|^2$ function features periodic variations in Q , where maxima occur at $Q \simeq k\pi/R$, with k being a positive integer¹⁸.

Figure 1 shows two sets of 1D SAXS data, one (black circles) from AuNP of nominal diameter 10 nm, and the other (red squares) of nominal diameter 5 nm. The nearly periodic variations in intensity are visible in both cases, and are inversely proportional to the particle size, consistent with Eq. (1). The dashed-lines in Fig. 1 are calculated intensity profiles for mono-disperse spheres that capture the intensity maxima to the largest extent. The smeared intensity minima of the SAXS data indicate a modest poly-dispersity in size distribution of AuNPs. Due to the lack of a deterministic way of knowing the polydispersity associated with the AuNPs, we only assume the radii of the AuNPs obey a Gaussian distribution $D(R)$, i.e., $D(R) = 1/(\sqrt{2\pi}\Delta R) \exp[-(R - \langle R \rangle)^2/(2\Delta R^2)]$, where $\langle R \rangle$ and ΔR represent the mean and the spread of the particle radii, respectively. The total intensity, $I(Q)$, from such a collection of particles, is expressed as¹⁹

$$I(Q) = \langle |\mathcal{F}|^2 \rangle = C \int |\mathcal{F}(Q, R)|^2 D(R) dR \quad (2)$$

where C denotes an intensity scale factor.

Profile-fitting in terms of Eq. (2) provides $\langle R \rangle$ and ΔR , as is summarized in Table 1. The mean diameter for the large particle group is smaller than the nominal value, in contrast to that for the small particle group. According to Eq. (2), the larger the particle, the more weight it carries in the total intensity. The dashed lines in Fig. 1 that match the intensity maxima are calculated for monodisperse spheres of radius approximately equal to $\langle R \rangle + \frac{1}{2}\Delta R$. Therefore, the intensity maxima still provide a good estimate of the particle size.

The SAXS intensity profiles of the DNA-coated AuNPs (data not shown), after scaling, are identical to those of bare AuNPs, indicating the X-rays are insensitive to the DNA outer-shell whose electron density is too close to that of the aqueous environment.

X-ray Reflectivity (XRR). Insoluble amphiphiles, such as DPTAP, after being spread on aqueous surfaces and compressed into a relatively densely packed state, form a Langmuir monolayer characteristic of stratified structure, i.e., a hydrophobic stratum for its hydrocarbon chains and a hydrophilic stratum for its polarized head-groups²⁰. Its vertical, stratified structure, manifested as the electron density (ED) depth profile, $\rho(z)$, across the interface and along the normal to the aqueous surface, can be determined by the specular XRR technique^{17,21}.

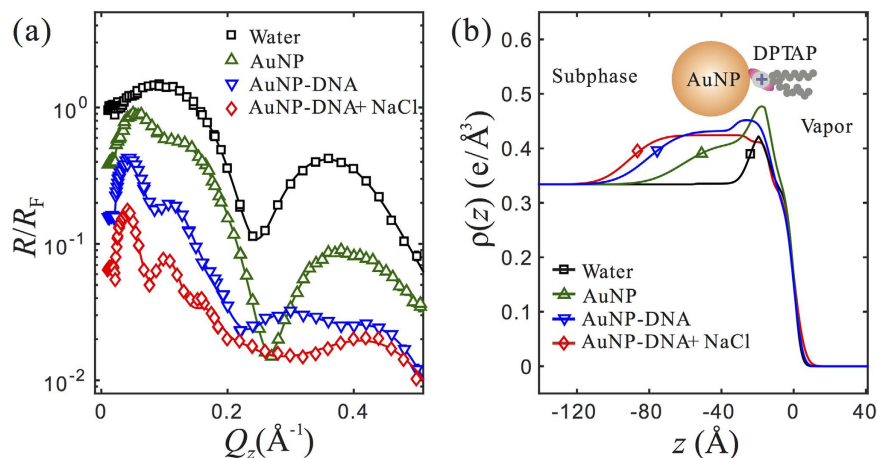


Figure 2. (a) R/R_F data for DPTAP monolayers spread on water subphase (\square), subphase containing AuNPs (10 nm in nominal diameter) of bare surface (Δ), AuNPs (10 nm in nominal diameter) coated with DNA (∇) and in the presence of 0.1 M NaCl (\diamond). The $R/R_F \approx 1$ at $Q_z < 0.0218 \text{ \AA}^{-1}$ and the data are shifted vertically for clarity. Solid lines are best-fit calculated reflectivities based on the refined parameters. (b) The corresponding electron density profiles across the air-water interface based on the best-fit structural parameters.

The XRR data, R , after being normalized to the calculated Fresnel reflectivity R_F for an ideally smooth and sharp air-water interface, are related to the corresponding interfacial ED profiles through structural refinement. To this end, a parametrized, continuous ED profile is constructed based on an appropriate structural model and further refined through comparison of its calculated reflectivity to the experimental data^{21,22}. In this study, the effective-density model is employed for the ED profile construction²². The calculation of the reflectivity of a given ED profile is based on the Parratt's recursive method¹⁷.

Figure 2 shows the R/R_F data for a DPTAP monolayer on various subphases under otherwise identical conditions of AuNP (10 nm nominal diameter of bare and capped with ssDNA) solutions. The R/R_F data for the DPTAP monolayer on a pure water subphase features fringes with two maxima at $Q_z \approx 0.09$ and 0.36 \AA^{-1} and the first minimum at $Q_z \approx 0.24 \text{ \AA}^{-1}$, which is similar to previously obtained XRR for DPTAP on pure water (albeit measured at relative higher surface pressure) using an in-house reflectometer²⁰. Qualitatively, if the monolayer is viewed as a single homogeneous slab of thickness L , R/R_F fringes are known as the Kiessig fringes corresponding to $L \approx 2\pi/\Delta Q_z \approx 23 \text{ \AA}$, ΔQ_z being the separation of the two consecutive maxima in Q_z ¹⁷. In a subtler model, the monolayer is viewed as constituted by two slabs of different ED, i.e. a slab for head groups (of thickness $l_H \approx 12 \text{ \AA}$ ²⁰) and the other for tail groups (of thickness $l_T \approx 13 \text{ \AA}$ ²⁰). In such case, $(l_H/2 + l_T) \approx 3\pi/(2Q'_z) \approx 20 \text{ \AA}$, Q'_z being the first reflectivity minimum in Q_z ²³.

The above semi-quantitative estimate is consistent with the corresponding ED profile constructed in terms of the best-fit structural parameters as shown in Fig. 2. On the ED profiles, the subphase, the head group, tail group and the vapor phase are readily recognized. In the presence of the AuNPs (nominal 10 nm diameter) in the subphase, the R/R_F profiles differ significantly from that for a mere water subphase. The first R/R_F maximum shifts to a much lower Q_z approximately 0.04 \AA^{-1} , indicating the formation of thickened layers. The new R/R_F maxima, lacking obvious periodicity as commonly seen in Kiessig fringes, can only be accounted for by a finer ED depth profiles, as shown in Fig. 2(b). Compared to the ED profile for the DPTAP on water, the presence of AuNPs in the subphase solutions results in significant ED enhancement in an extensive portion across $\sim 50\text{--}100 \text{ \AA}$ immediately below the monolayer-subphase interface. Indeed, at neutral pH DPTAP monolayer is positively charged while surface charge of bare AuNPs is negative with corresponding Zeta potential of -40.6 mV . The bare AuNPs bind to DPTAP monolayer through electrostatic interaction and enrich the surface ED. Considering the diameter of the AuNPs of bare surface is $\lesssim 100 \text{ \AA}$, this is evidence that the AuNPs adsorbed underneath the monolayer form a single layer. The DNA surface coating and further the presence of NaCl both facilitate the AuNPs surface adsorption, as evidenced by the relatively more extended in thickness and uniform adsorption layer on the ED profiles. We note that based on the average ED extracted from the X-ray reflectivity we conclude that the surface is not fully covered by AuNPs (assuming the cross section a AuNP is approximately 100 nm^2 , we estimate a 5 to 10% surface coverage consistent with the GISAXS discussed below).

Grazing incidence small-angle scattering (GISAXS). The XRR indicates that the surface adsorbed AuNPs is restricted within a single layer. Figure 3 shows two representative GISAXS intensity contour plots as a function of Q_y and Q_z . Both contours feature an intensity maximum at low $Q_y - Q_z$ regime, of which the origin is to be explored. There is also a second intensity maximum on a ridge at $Q = 0.1 - 0.15 \text{ \AA}^{-1}$, where $Q = \sqrt{Q_z^2 + Q_y^2}$. For the AuNPs of bare surface, the ridge is on a broken ring of radius $Q \approx 0.13 \text{ \AA}^{-1}$, along which there are two intensity maxima at $Q_z \approx 0.02$ and 0.12 \AA^{-1} . For the AuNPs coated with DNA, the ridge almost coincides with a ring of radius $Q \approx 0.12 \text{ \AA}^{-1}$.

Figure 4 shows the GISAXS intensity at $Q_z \approx 0.02 \text{ \AA}^{-1}$ that is enhanced significantly due the surface multiple scattering^{17,24}. The intensity maxima coincide well with $|\mathcal{F}|^2$ for a solid sphere of radius R that is close to the nominal

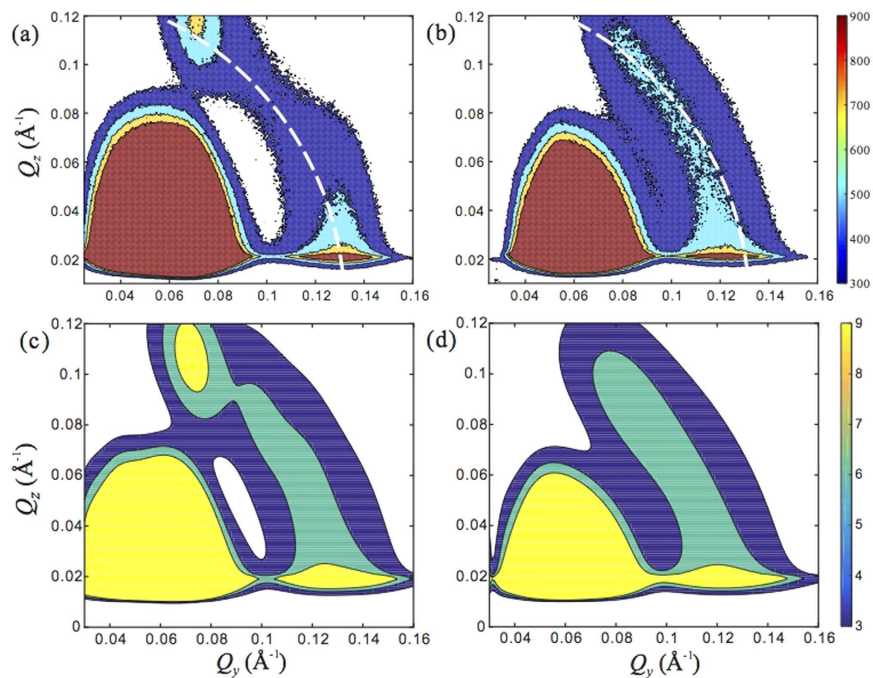


Figure 3. Two-dimensional contour maps for GISAXS intensity as function of Q_z and Q_y , for (a) AuNPs of bare surface (10 nm in nominal diameter) (b) AuNPs (10 nm in nominal diameter) coated with DNA, both with DPTAP monolayers. The white dashed lines are an arc at $|\mathbf{Q}| = \sqrt{Q_z^2 + Q_y^2} = 0.13 \text{ \AA}^{-1}$. (c,d) Simulated 2D GISAXS intensity contours for (a,b), respectively.

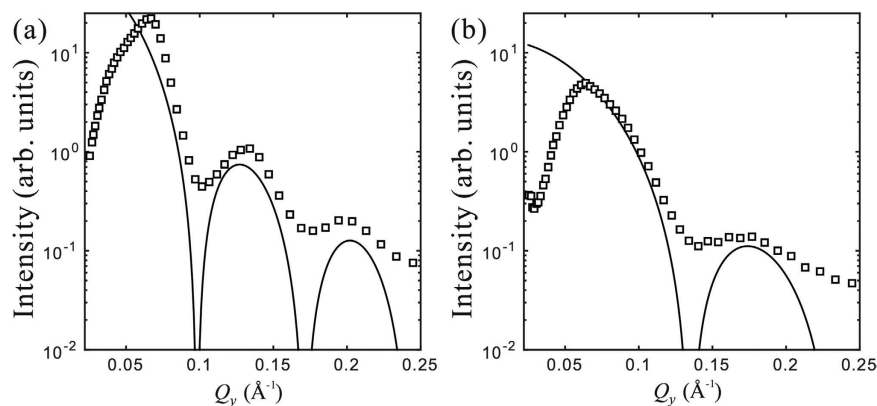


Figure 4. GISAXS intensity (\square) as function of Q_y , at $Q_z = 0.02 \text{ \AA}^{-1}$ for DPTAP monolayers on subphases containing (a) AuNPs of nominal radius 50 Å and (b) AuNP of nominal radius 25 Å. The solid lines are the $|\mathcal{F}(\mathbf{Q})|^2$ (vertically shifted for display purpose) for a solid sphere of radius 45 Å in (a) and 33 Å in (b) at $Q_z = 0.02 \text{ \AA}^{-1}$ and $Q_x \approx 0$.

radius of the AuNP. As the $|\mathcal{F}|^2$ approach the maximum at $Q=0$, the suppression of the intensity at low Q_{xy} indicates strong particle-particle interference arising from close packing^{25–27}. The smearing of the sharp intensity minima present in the SAXS from monodisperse spheres is consistent with the polydispersity found in bulk SAXS shown in Fig. 1.

The quantitative GISAXS analysis is complex in general²⁴. In this study, a simplistic, crude approximation, so called local monodisperse approximation (LMA), is adopted^{25,28}. The LMA approximation states that the GISAXS intensity can be viewed as an incoherent sum of the intensities arising from coherently illuminated domains, each of which contains monodispersely distributed and spatially correlated particles, as illustrated in Fig. 5. Accordingly, the GISAXS intensity, $I(Q_{xy}, Q_z)$, from one such domain consisting of identical spheres, can be expressed as^{24–26,29,30}

$$I(Q_{xy}, Q_z) = C \cdot |\mathcal{F}|^2 \cdot S(Q_{xy}, Q_z) \quad (3)$$

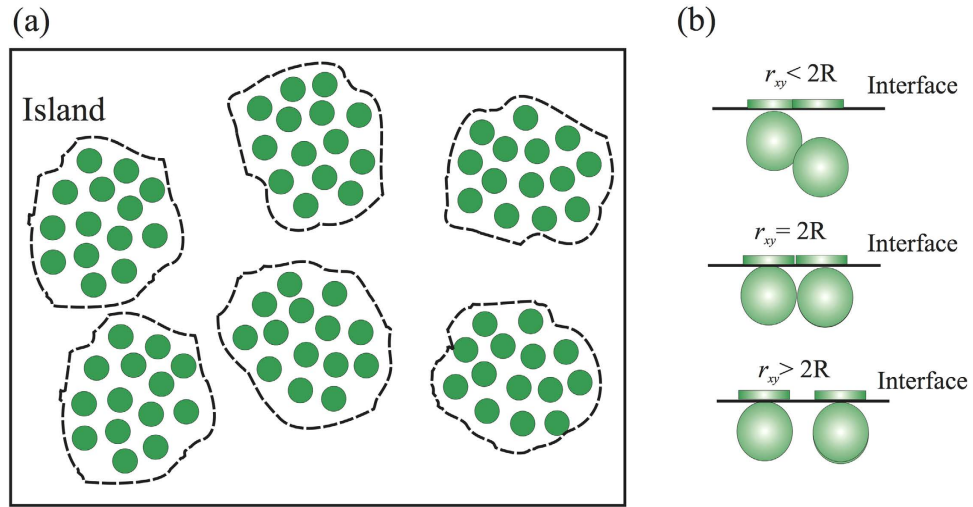


Figure 5. Surface covered by islands, each of which contains short range ordered, identical spheres. Island boundary is represented by the dashed line that encloses the spheres. The average surface density of spheres within an island is denoted as $\langle n \rangle$. (b) Schematic scenarios showing relative position of two particles and their corresponding projection onto the surface.

where C is an intensity scale factor. $S(Q_{xy}, Q_z)$ represents the interference function of the spheres with the form factor \mathcal{F} and is solely dependent on their relative positions^{17,26}. Q_{xy} is the magnitude of the in-plane component of the scattering vector, and $Q_{xy} = \sqrt{Q_x^2 + Q_y^2} \approx Q_y$ as $Q_x \approx 0$. Assuming all domains share the same $S(Q_{xy}, Q_z)$ and replacing $|\mathcal{F}|^2$ with $\langle |\mathcal{F}|^2 \rangle$ in Eq. (3), $I(Q_{xy}, Q_z)$ thus can represent the GISAXS intensity averaged over all domains.

For distribution of particles in 3D space^{17,26}, $S(Q_{xy}, Q_z)$ is expressed as follows

$$S(Q_{xy}, Q_z) = 1 + \int_V [\rho_n(r_{xy}, z) - \langle \rho_n \rangle] \cdot \exp[iQ_{xy} \cdot r_{xy} + iQ_z \cdot z] dV \quad (4)$$

where V and dV represent the domain volume and the corresponding differential volume element, $\rho_n(r_{xy}, z)$ the local number density of spheres at the (r_{xy}, z) position, and $\langle \rho_n \rangle$ the average number density of the spheres in the domain.

In the analysis, only the slice of intensity parallel to the surface is analyzed (i.e., at $Q_z = 0.02 \text{ \AA}^{-1}$). As Q_z is very close to zero, Eq. (4) is rewritten as

$$S(Q_{xy}, Q_z \rightarrow 0) = 1 + \int_A \underbrace{\left\{ \int [\rho_n(r_{xy}, z) - \langle \rho_n \rangle] dz \right\}}_{\text{Projection: 3D} \rightarrow \text{2D}} \cdot \exp[iQ_{xy} \cdot r_{xy}] dA \quad (5)$$

where A and dA represent the domain area and the corresponding differential area element. The integration enclosed in the curly brackets is the projection of the 3D density function onto the 2D plane (i.e., x - y plane), illustrated in Fig. 5(b). The range of projected distance between a pair of spheres in contact, r_{xy} , is between zero and $2R$, depending on the relative orientation.

Let $S_{2D}(Q_{xy})$ represent $S(Q_{xy}, Q_z \rightarrow 0)$ and rewrite Eq. (5) as follows,

$$S_{2D}(Q_{xy}) = 1 + 2\pi \langle n \rangle \int_0^\infty [g(r_{xy}) - 1] J_0(Q_{xy} r_{xy}) r_{xy} dr_{xy} \quad (6)$$

where the function $J_0(\cdot)$ is the zero order Bessel function of the first kind and $\langle n \rangle$ is the average number of spheres per unit area. The product of $g(r_{xy})$ and $\langle n \rangle$ gives the local number of spheres per unit area at a distance r_{xy} away from an arbitrarily chosen sphere center. The $g(r_{xy})$ thus represents the 2D radial distribution function of spheres projected onto the plane.

In view of Eqs (3–6), the GISAXS intensity at large Q_{xy} in Fig. 4 are clearly dominated by the form factor of the individual particles and $S_{2D}(Q_{xy}) \rightarrow 1$, while at small Q_{xy} , the intensity data is strongly suppressed by the $S_{2D}(Q_{xy})$. This feature in the 3D analog has been attributed to the short-range-order (SRO) among close-packed hard spheres that model liquid structures long ago by Kirkwood *et al.* via simulations^{26,31}. Still, a general, explicit formula of structure factor for liquid-like structures is not readily available as the corresponding radial distribution function is determined by interaction potentials among particles that are in general difficult to ascertain^{26,31}. Only a few structure factors are analytically available for certain inter-particle potential approximations (e.g., hard-sphere potential), by solving the Ornstein-Zernike (OZ) equation using the Percus-Yevick (PY) approximation^{32,33}. These explicit structure factors have been applied to 3D colloidal suspension systems, but rarely applied to an interfacial system. The determination of the structure factor for particles in liquid-like state confined

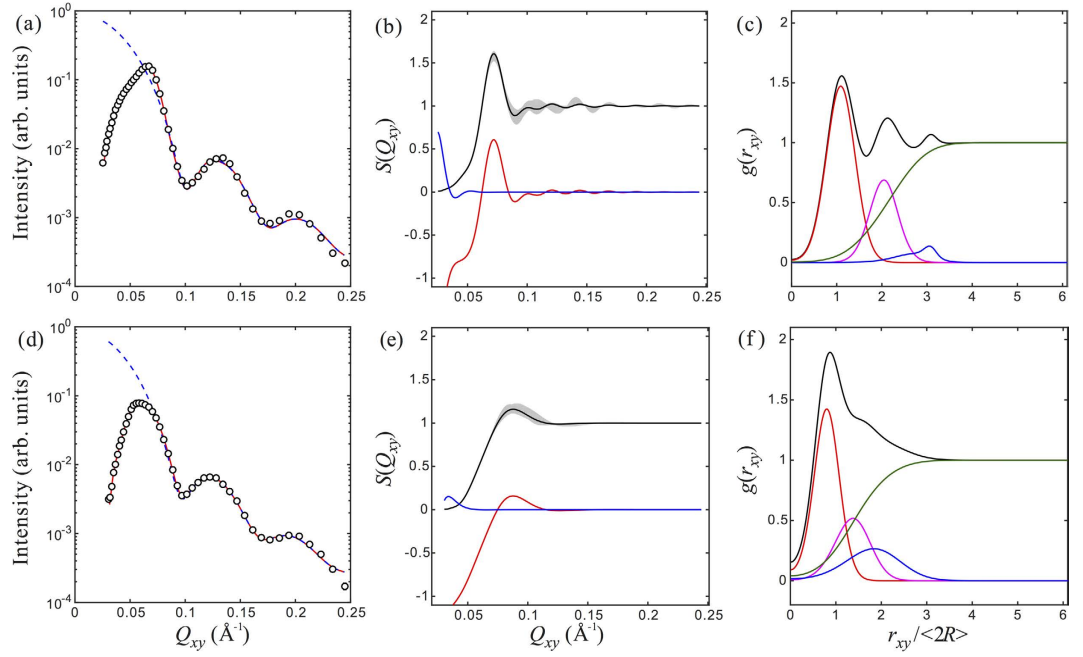


Figure 6. Data analysis for GISAXS intensity line-cut parallel to the surface (i.e., along Q_y -axis) for AuNPs without DNA-coating (top row) and AuNPs with DNA-coating (bottom row). (a,d) GISAXS line-cut intensity data (circles) obtained at $Q_z = 0.02 \text{ \AA}^{-1}$. The dashed lines are calculated, independent scattering intensity (i.e., $\langle |\mathcal{F}|^2 \rangle$) for a set of hypothetically uncorrelated spheres of given size distribution given in Table 1. The solid lines result from the multiplication of the $\langle |\mathcal{F}|^2 \rangle$ and the structure factor $S_{2D}(Q_{xy})$ shown in (b,e). (b,e) The ensemble averaged, positional structure factor $S_{2D}(Q_{xy})$. The shaded area indicates the variations of the local $S_{2D}(Q_{xy})$ profiles. The red lines are contributions from the countable (i.e., three) neighboring shells. The blue lines are contribution from the gas-like disorder term. (c,f) are radial distribution function directly converted from the ensemble averaged $S(Q_{xy})$ in (b,e). The red, magenta and blue lines are contributions from the first, second and third neighboring shells. The green lines are contribution from the gas-like disorder term.

in 2D space heretofore, stimulated by the fundamental study on 2D phase transition, still relies on numerical computations³⁴.

Another approach to deduce the structure factor is in the crystallographic manner by introducing disorders/imperfections into ideal crystal systems^{35,36}. Lazzari and Renaud *et al.* investigated similar features in GISAXS patterns from solid surfaces²⁷ and provided an empirical formula for $S_{2D}(Q_{xy})$ ²⁹. In a separate study, they also proposed a theoretical framework based on a classical 1D model (i.e., one-dimensional chain of correlated particles) to incorporate the particle size and spacing correlation into GISAXS analysis²⁵.

In this study, we start with the radial distribution function and further introduce disorder effects. The details are presented in the Supporting Information (SI). The structure factor only includes a contribution from a few neighboring shells, which usually is the case for a liquid-like structure. The derived $S_{2D}(Q_{xy})$, denoted as $S^{\text{SRO}}(Q_{xy})$, is expressed as follows,

$$S^{\text{SRO}}(Q_{xy}) = 1 + \sum_i Z_i \cdot J_0(Q_{xy} D_i) \cdot \exp(-Q_{xy}^2 \Lambda_i^2) + \frac{2\pi < n > \Lambda_{\text{cutoff}}}{Q_{xy}} J_1(Q_{xy} D_{\text{cutoff}}) \cdot \exp(-Q_{xy}^2 \Lambda_{\text{cutoff}}^2) \quad (7)$$

where Z_i and D_i are the coordination number and average 2D-projected distance of the i -th neighboring-shell (or annulus) around a central sphere. Λ_i is the 2D-projected, spatial spread of the i -th shell. $J_1(\cdot)$ is the first order Bessel function of the first kind. D_{cutoff} is the 2D-projected distance where the crystal-like structure transits to the gas-like structure (i.e., ordered structure to an utterly disorder) occurs and Λ_{cutoff} being the associated uncertainty in the boundary of order-to-disorder transition. Let $\Lambda_i = 0$, Eq. (7) is a 2D analog of the Debye formula for 3D powder diffraction that is commonly used to calculate the scattering from small crystals containing a few building units²⁶.

Figure 6 shows analysis of the data shown in Fig. 3 for AuNPs without DNA-coating (top row) and AuNPs with DNA-coating (bottom row), based on Eq. (7). The data shown in (a,d) are profile-fit with $S_{2D}(Q_{xy})$ (given in Eq. (7)) multiplied by $\langle |\mathcal{F}|^2 \rangle$ which has been obtained from the bulk SAXS data analysis. The corresponding profiles for $S_{2D}(Q_{xy})$ are shown in (b,e). The $S_{2D}(Q_{xy})$ profiles exhibit a main interference peak within $Q_{xy} = 0.05 - 0.1 \text{ \AA}^{-1}$, for surface NP assemblies. The main interference peak for AuNP in the absence of surface DNA-coating appears more pronounced than in the presence of DNA-coating. Indeed, the main interference

Samples	Bare AuNPs	DNA-AuNPs
Z_1	9.0 ± 1.1	6.0 ± 1.4
D_1 (Å)	99 ± 2	76 ± 2
Λ_1/D_1	0.2	0.2
Z_2	8 ± 3	4.9 ± 1.2
D_2/D_1	1.8 ± 0.1	1.7 ± 0.1
Λ_2/D_1	0.2	0.3
D_{cutoff}/D_1	2.0 ± 0.2	1.8 ± 0.3
$\Lambda_{\text{cutoff}}/D_1$	0.4 ± 0.1	0.5 ± 0.1

Table 2. Structural parameters determined by GISAXS^{a,b,c}. ^aInclusion of the parameter Z_3 , D_3 and Λ_3 can improve the profile fitting, but is not essential. ^bThe data fitting is not sensitive to the parameter $\langle n \rangle$. Thus the $\langle n \rangle$ is allowed to vary in the $1.5 \pm 0.5 \times 10^{-4} \text{ \AA}^{-2}$ range. ^cThe contribution of gas-like disorder is mainly restricted to low Q_{xy} regime. The larger the D_{cutoff} , the lower the Q_{xy} regime it dictates. So only the lower limit of the D_{cutoff} is considered in this study.

peak within the Q_{xy} window is mainly composed of the contributions from the neighboring shells, rather than the gas-like structure. In (c) and (f), the corresponding $g(r_{xy})$ profiles are displayed, where the contribution from “crystal-like structure” and “gas-like structure” are shown. It appears that one can still identify the nearest neighbor and/or next nearest neighbor shells for bare AuNPs. In contrast, it is impossible to distinguish the 1st and 2nd nearest neighbor shells for AuNP coated with DNA. If we assume $S(Q_{xy}, Q_z) = S_{2D}(Q_{xy})$ and include the multiple scattering effects, we can regenerate the full GISAXS map, as shown in Fig. 3(c,d) for both samples. The similarity between the measured GISAXS patterns in Fig. 3 and the calculations are pretty good indicating the Q_z dependence in $S(Q_{xy}, Q_z)$ is nearly constant within the Q_z range measured. A complete Q_z -independence corresponds to an absolute Dirac-delta $\delta(z)$ distribution of spheres. Our analysis also shows that the gas-like disorder term is not essential in fitting data within the current Q_{xy} range. This can be seen in Fig. 6(b,e) where the corresponding contribution from the gas-like disorder term is limited to extremely small Q_{xy} and almost zero at large Q_{xy} . In Table 2 we list the structural parameters that are used to generate the model calculations shown in Fig. 6. These same parameters are used to simulate the 2D GISAXS patterns (Fig. 3(c,d)) that capture the experimental features adequately. We note that this approach to analyzing the GISAXS for general 2D systems with SRO is in fact the 2D analog to the Debye formula for 3D XRD of finite size crystals²⁶.

Conclusion

Using surface sensitive diffraction methods, i.e., X-ray reflectivity and grazing incidence X-ray small-angle scattering, we demonstrate that bare (unfunctionalized) gold nanoparticles (AuNP) are negatively charged and spontaneously adsorb to a cationic lipid template formed by a Langmuir monolayer (in this case formed by DPTAP (1,2-dihexadecanoyl-3-trimethylammonium-propane). The XRR yields the density profile across the charged-surface normal and shows that the AuNPs assemble as a single layer that is contiguous to the DPTAP monolayer. The analysis of the GISAXS in terms of a structure factor of loosely packed 2D particles indicates that the adsorbed AuNP monolayer exhibits short-range in-plane correlations. By contrast single-stranded-DNA-functionalized AuNPs, while attracted to the positively charged surface (more efficiently with the addition of NaCl to the solution) display less regular two-dimensional packing compared to bare AuNPs. Our results and analysis demonstrate that the behavior of AuNPs can be manipulated in a similar fashion to manipulating negatively charged ions. This opens a new avenue for assembly of nanoparticles by designing charged templates. Exploiting electrostatic forces is also relevant to functionalization of nanoparticles with charged entities such as polyelectrolytes to form shells with diverse functionalities. In addition, we provide a new approach to analyzing the GISAXS data for short-range-ordered particles in two-dimensions that directly yields the 2D pair-distribution function.

Methods

Reagents and Materials. 1,2-dihexadecanoyl-3-trimethylammonium-propane (DPTAP) was purchased from Avanti Polar Lipids, Inc as powders and dissolved in 3:1 chloroform/methanol solution for Langmuir monolayer deposition. Gold nanoparticles with nominal size of 5 and 10 nm in diameter were purchased from Ted Pella, Inc and their actual size was determined by small-angle X-ray scattering (SAXS). Non-complementary single-stranded DNA capped gold nanoparticles (DNA-AuNPs) were synthesized according to the documented procedures in the literature with slight modifications^{37–40}. The 5'-thiolated single-stranded DNA with 28 bases (sequence: 5'-SH-(CH₂)₆-TTT TTT GTG GAA AGT GGC AAT CGT GAA G-3') was purchased from Integrated DNA Technologies as disulfides. The DNA with disulfide bonds was cleaved with dithiothreitol (Pierce Biotechnology, Thermo Scientific), purified with NAP-5 column (Sephadex G-25 DNA grade, GE Healthcare) and incubated with AuNPs solutions (nominal size 10 nm) under shaking at room temperature. The mixture of freshly cleaved DNA and AuNPs was then buffered with sodium phosphate (pH 7.0) followed by a slow salting process, in which the concentration of NaCl in the mixtures was gradually increased to 0.5 M over 2 days. The final mixture was aged at room temperature for another day and washed with Millipore water (18.2 MΩ·cm) by centrifugation (20000 g × 1 h) at least three times. DNA-AuNPs were dispersed in Millipore water and the concentration was determined with a UV-visible spectrophotometer. Unfunctionalized and DNA functionalized AuNPs at concentrations of 9 and 1 nM were used for the X-ray measurements, respectively.

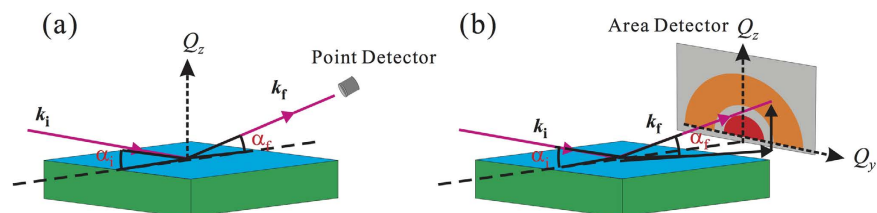


Figure 7. Schematic of setup for X-ray (a) reflectivity and (b) grazing incidence small-angle scattering.

Experimental setup. Grazing incidence small-angle X-ray scattering (GISAXS) and reflectivity (XRR) measurements were carried out on the liquid surface spectrometer (LSS) at the 9-IDB beamline Advanced Photon Source (APS), Argonne National Laboratory. The highly monochromatic X-ray beam of energy $E = 13.474$ keV (corresponding wavelength $\lambda = 0.9201$ Å) yields a critical incident-angle for total reflection, $\alpha_c = 0.0915^\circ$. A schematic illustration of the X-ray experimental setup is shown in Fig. 7. For an XRR measurement, a Bicron point detector is used to collect reflected beam at an exit angle $\alpha_r = \alpha_i$ in the scattering plane (defined by the surface normal (z -axis) and the incident beam). The reflectivity is measured as a function of the z -component of the scattering vector \mathbf{Q} , i.e. $Q_z = (4\pi/\lambda) \sin \alpha_i$. For a GISAXS measurement, a digital, two-dimensional Pilatus 100 K detector (487×195 pixels, 172×172 μm per pixel) has been placed 2041 mm away (downstream) from the aqueous surface (sample) center. The scattering vector, \mathbf{Q} , for GISAXS data, is calibrated with a diffraction pattern obtained from a standard silver-behenate powder. The three components of the scattering vector, i.e., (Q_x, Q_y, Q_z) , are normal to one another and are defined in such way that the Q_z component is along the surface normal while Q_x and Q_y components are within the surface. For GISAXS, Q_y is conventionally defined as parallel to the surface of detector for $Q_x \approx 0$. Therefore, the magnitude of the in-plane scattering vector, Q_{xy} , defined as $\sqrt{Q_x^2 + Q_y^2}$, is approximately equivalent to Q_y . Analysis methodology is provided in detail in the SI and elsewhere^{41,42}. The DPTAP monolayer is spread on aqueous nanoparticle suspension that is contained in an enclosed thermostated Teflon Langmuir trough (dimension 60 mm by 60 mm). The monolayer compression is performed with a motorized Teflon bar and surface pressure is measured with a Wilhelmy plate. The trough canister is sealed and purged with water-saturated helium gas in which the oxygen level is monitored with a sensor (S101, Qubit System Inc.) during the X-ray measurements (waiting time before measurements 0.5–1 hour). The temperature in the trough is kept constant at 20 °C.

Small-angle X-ray scattering (SAXS) in transmission mode has been performed at beamline 12ID-B, APS, on dilute AuNP bulk solutions to determine the actual size and distribution of the particles in the suspension. For these experiments, the AuNPs solutions were loaded in a flow cell that is vertically mounted normal to the incident X-ray beam (X-ray energy $E = 14.0$ keV). A 2D detector Pilatus2m was used and the scattering vector magnitude Q was calibrated with silver behenate powder low-angle diffraction. Various concentrations of AuNPs were examined to ensure independent scattering from particles. The 2D SAXS images were then converted to 1D data through radial average and further corrected for background subtraction and intensity normalization¹⁹.

References

- Kaganer, V. M., Möhwald, H. & Dutta, P. Structure and phase transitions in Langmuir monolayers. *Rev. Mod. Phys.* **71**, 779–819 (1999).
- Pershan, P. S. & Schlossman, M. L. *Liquid Surface and Interfaces: Synchrotron X-ray Methods* (Cambridge University Press, 2012).
- Kuzmenko, I. *et al.* Design and characterization of crystalline thin film architectures at the air-liquid interface: simplicity to complexity. *Chem. Rev.* **101**, 1659–1696 (2001).
- Pieranski, P. Two-dimensional interfacial colloidal crystals. *Phys. Rev. Lett.* **45**, 569–572 (1980).
- Onoda, G. Y. Direct observation of two-dimensional, dynamical clustering and ordering with colloids. *Phys. Rev. Lett.* **55**, 226–229 (1985).
- Kepler, G. M. & Fraden, S. Attractive potential between confined colloids at low ionic strength. *Phys. Rev. Lett.* **73**, 356–359 (1994).
- Marcus, A. H. & Rice, S. A. Observation of first-order liquid-to-hexatic and hexatic-to-solid phase transition in a confined colloid suspension. *Phys. Rev. Lett.* **77**, 2577–2580 (1997).
- Ramos, L., Lubensky, T. C., Dan, N., Nelson, P. & Weitz, D. A. Surfactant-mediated two-dimensional crystallization of colloidal crystals. *Science* **286**, 2325–2328 (1999).
- Whitesides, G. M. & Grzybowski, B. Self-assembly at all scales. *Science* **295**, 2418–2421 (2002).
- Pfeiffer, C. *et al.* Interaction of colloidal nanoparticles with their local environment: the (ionic) nanoenvironment around nanoparticles is different from bulk and determines the physico-chemical properties of the nanoparticles. *J. R. Soc. Interface* **11**, 20130931 (2014).
- Zhang, X., Servos, M. R. & Liu, J. Ultrahigh nanoparticles stability against salt, pH, and solvent with retained surface accessibility via depletion stabilization. *J. Am. Chem. Soc.* **134**, 9910–9913 (2012).
- Cheng, W. *et al.* Probing in Real Time the Soft Crystallization of DNA-Capped Nanoparticles. *Angew. Chem., Int. Ed.* **49**, 380–384 (2010).
- Campolongo, M. J. *et al.* Crystalline Gibbs Monolayers of DNA-Capped Nanoparticles at the Air-Liquid Interface. *ACS Nano* **5**, 7978–7985 (2011).
- Tan, S. J. *et al.* Crystallization of DNA-Capped Gold Nanoparticles in High-Concentration, Divalent Salt Environments. *Angew. Chem., Int. Ed.* **53**, 1316–1319 (2014).
- Srivastava, S., Nykypanchuk, D., Fukuto, M. & Gang, O. Tunable nanoparticle arrays at charged interfaces. *ACS Nano* **8**, 9857–9866 (2014).
- Srivastava, S. *et al.* Two dimensional DNA-programmable assembly of nanoparticles at liquid interfaces. *J. Am. Chem. Soc.* **136**, 8323–8332 (2014).
- Als-Nielsen, J. & McMorrow, D. *Elements of Modern X-ray Physics* (John Wiley & Sons, 2011).

18. Roe, R. *Methods of X-ray and Neutron Scattering in Polymer Science* Ch. 5 (Oxford University Press, 2000).
19. Zhang, H. *et al.* Morphological transformations in the magnetite biomimetic protein Mms6 in iron solutions: A small-angle X-ray scattering study. *Langmuir* **31**, 2818–2825 (2015).
20. Sung, W., Wang, W., Lee, J., Vaknin, D. & Kim, D. Specificity and variation of length scale over which monovalent halide ions neutralize a charged interface. *J. Phys. Chem. C* **119**, 7130–7137 (2015).
21. Vaknin, D. X-Ray diffraction techniques for liquid surfaces and monomolecular layers. In *Characterization of Materials* (ed. Kaufmann, E. N.) Vol. 2, 1393–1423 (John Wiley & Sons, 2012).
22. Tolan, M. *X-Ray Scattering from Soft-Matter Thin Films: Materials Science and Basic Research* (Springer-Verlag, 1999).
23. Kjaer, K. Some simple ideas on X-ray reflection and grazing incidence diffraction from thin surfactant films. *Physica B* **198**, 100–109 (1994).
24. Renaud, G., Lazzari, R. & Leroy, F. Probing surface and interface morphology with grazing incidence small angle X-ray scattering. *Surf. Sci. Rep.* **64**, 255–380 (2009).
25. Lazzari, R., Leroy, F. & Renaud, G. Grazing-incidence small-angle x-ray scattering from dense packing of islands on surfaces: Development of distorted wave Born approximation and correlation between particle sizes and spacing. *Phys. Rev. B* **76**, 125411 (2007).
26. Guinier, A. *X-Ray Diffraction in Crystals, Imperfect Crystals and Amorphous Bodies* Ch. 2 (Dover Publication Inc., 1994).
27. Renaud, G. *et al.* Real-time monitoring of growing nanoparticles. *Science* **300**, 1416–1419 (2003).
28. Gazzillo, D., Giacometti, A., Valle, R. G. D., Venuti, E. & Carsughi, F. A scaling approximation for structure factors in the integral equation theory of polydisperse nonionic colloidal fluids. *J. Chem. Phys.* **111**, 7636–7645 (1999).
29. Lazzari, R., Renaud, G., Revenant, C., Jupille, J. & Borensztein, Y. Adhesion of growing nanoparticles at a glance: Surface differential reflectivity spectroscopy and grazing incidence small angle x-ray scattering. *Phys. Rev. B* **79**, 125428 (2009).
30. Hexemer, A. & Müller-Buschbaum, P. Advanced grazing-incidence techniques for modern soft-matter materials analysis. *IUCr* **2**, 106–125 (2015).
31. Chandler, D. *Introduction to Modern Statistical Mechanics* (Oxford University Press, 1987).
32. Kaler, E. W. Small angle scattering from complex fluids. In *Modern Aspects of Small-Angle Scattering* (ed. Brumberger, H.) (Kluwer Academic Publishers, 1995).
33. Chen, S.-H. & Tartaglia, P. *Scattering Methods in Complex Fluids* (Cambridge University Press, 2015).
34. Asgari, R., Davoudi, B. & Tanatar, B. Hard-core Yukawa model for two-dimensional charge-stabilized colloids. *Phys. Rev. E* **64**, 041406 (2001).
35. Senesi, A. J. & Lee, B. Small-angle scattering of particle assemblies. *J. Appl. Cryst.* **48**, 1172–1182 (2015).
36. Welberry, T. R. *Diffuse X-ray Scattering and Models of Disorder* (Oxford University Press, 2010).
37. Hill, H. D. & Mirkin, C. A. The bio-barcode assay for the detection of protein and nucleic acid targets using DTT-induced ligand exchange. *Nat. Protoc.* **1**, 324–336 (2006).
38. Hurst, S. J., Lytton-Jean, A. K. R. & Mirkin, C. A. Maximizing DNA Loading on a Range of Gold Nanoparticle Sizes. *Anal. Chem.* **78**, 8313–8318 (2006).
39. Maye, M. M., Nykypanchuk, D., van der Lelie, D. & Gang, O. A Simple Method for Kinetic Control of DNA-Induced Nanoparticle Assembly. *J. Am. Chem. Soc.* **128**, 14020–14021 (2006).
40. Maye, M. M., Nykypanchuk, D., Cuisinier, M., van der Lelie, D. & Gang, O. Stepwise surface encoding for high-throughput assembly of nanoclusters. *Nat. Mater.* **8**, 388–391 (2009).
41. Dimon, P. *et al.* Structure of aggregated gold colloids. *Phys. Rev. Lett.* **57**, 595–598 (1986).
42. Bracewell, R. *The Fourier Transform and Its Applications* (McGraw-Hill, 1999).

Acknowledgements

We thank Xiaobin Zuo at beamline 12ID-B, APS, for technical support in measuring bulk SAXS. H. Z. thanks Prof. Mufit Akinc (Ames Laboratory and Iowa State University) for discussion on functionalization of AuNPs with DNA. Research was supported by the U.S. Department of Energy, Office of Basic Energy Sciences, Division of Materials Sciences and Engineering. Ames Laboratory is operated for the U.S. Department of Energy by Iowa State University under Contract No. DE-AC02-07CH11358. Use of the Advanced Photon Source, an Office of Science User Facility operated for the U.S. Department of Energy (DOE) Office of Science by Argonne National Laboratory, was supported by the U.S. DOE under Contract No. DE-AC02-06CH11357.

Author Contributions

D.V., W.W. and S.M. conceived the experiments; H.Z., W.W. and D.V. conducted the experiments; I.K. provided technical support at the APS; W.W. analyzed the data with the help of D.V.; W.W., H.Z. and D.V. wrote the manuscript. All authors reviewed the manuscript.

Additional Information

Supplementary information accompanies this paper at <http://www.nature.com/srep>

Competing financial interests: The authors declare no competing financial interests.

How to cite this article: Wang, W. *et al.* Assembling Bare Au Nanoparticles at Positively Charged Templates. *Sci. Rep.* **6**, 26462; doi: 10.1038/srep26462 (2016).



This work is licensed under a Creative Commons Attribution 4.0 International License. The images or other third party material in this article are included in the article's Creative Commons license, unless indicated otherwise in the credit line; if the material is not included under the Creative Commons license, users will need to obtain permission from the license holder to reproduce the material. To view a copy of this license, visit <http://creativecommons.org/licenses/by/4.0/>